Thermo-responsive nano-in-micro particles for MRI-guided chemotherapy

Ziwei Zhang[a,b], Yuexin Wang[a], Marwa M. I. Rizk[a,b,c], Ruizheng Liang[e], Connor J. R. Wells[b], Pratik Gurnani[d], Fenglei Zhou[f], Gemma-Louise Davies[b,*], and Gareth R. Williams[a,*]

[a] UCL School of Pharmacy, University College London, 29 – 39 Brunswick Square, London WC1N 1AX, UK

[b] UCL Department of Chemistry, University College London, 20 Gordon St, London WC1H 0AJ, UK

[c] Department of Pharmaceutics, Faculty of Pharmacy, Alexandria University, Alexandria, Egypt

[d] Division of Molecular Therapeutics and Formulation, School of Pharmacy, University Park, University of Nottingham, Nottingham, NG7 2RD

[e] State Key Laboratory of Chemical Resource Engineering, Advanced Innovation Center for Soft Matter Science and Engineering, Beijing University of Chemical Technology, Beijing 100029, China.

[f] Centre for Medical Image Computing, University College London, 90 High Holborn, London WC1V 6LJ, UK

* Authors for correspondence. Email: gemma-louise.davies@ucl.ac.uk (GLD); g.williams@ucl.ac.uk (GRW). Tel: +44(0) 207 679 7524 (GLD); +44(0) 207 753 5868 (GRW)

Abstract

In this work, we develop nano-in-micro thermo-responsive microspheres as theranostic systems for anti-cancer hyperthermia. Firstly, layered double hydroxide (LDH) nanoparticles were synthesized and subsequently loaded with the chemotherapeutic agents methotrexate (MTX) or 5-fluorouracil (5FU). The drug-loaded LDH particles were then co-encapsulated with superparamagnetic iron oxide nanoparticles (SPIONs) into poly(acrylamide-co-acrylonitrile) microparticles *via* spray drying. The SPIONs are able to act as MRI contrast agents, thus resulting in potential theranostic formulations. Concave microparticles were observed by electron microscopy, and elemental mapping results suggest the LDH and SPION particles were homogeneously distributed inside the microparticles. *In vitro* dissolution tests showed that the drug was released over a prolonged period of time with the microspheres having distinct release curves at 37 and 43 °C, and the relaxivity (r_2) profile microparticles were also found to be different over the temperature range 35 to 46 ºC, both reflecting obvious thermo-responsive properties. Mathematical relationships between r_2, release and temperature data

were established, demonstrating that the microparticles have the potential for use in MRI-guided therapy. *In vitro* cell experiments revealed that the formulations permit synergistic hyperthermia-aided chemotherapy in cultured Caco-2 and A549 cells. Thus, the microparticles prepared in this work have potential as smart stimuli-responsive theranostics for hyperthermia-aided chemotherapy.

Statement of significance

Hyperthermia is an effective treatment for cancer, enabling an elevation of tumor temperature to promote other treatments such as chemotherapy or radiotherapy. However, high temperatures can be harmful to healthy surrounding tissues, while the damage induced by mild thermal treatment (42-45 °C) tends to be repaired by cancer cells' intrinsic thermoresistance systems. A series of thermo-responsive particles are designed in this work for magnetic resonance imaging (MRI)-aided synergistic thermal-chemotherapy, which could overcome these bottlenecks in the applications of hyperthermia. The thermo-responsive microparticles are constructed by combining anticancer agent loaded nanoparticles and MRI contrast agents into temperature-responsive polymer microspheres. These nano-in-micro formulations allow a rapid release of their chemotherapeutic cargo at moderate hyperthermia conditions (43 °C), thus dramatically enhancing cytotoxic efficacy. Moreover, the MRI properties of the microspheres also displayed a thermo-responsive behaviour, which can be used to temporally and spatially monitor the temperature and drug release during treatment. Thus, our formulations could potentially work as novel theranostic platforms to integrate the MRI imaging with anticancer treatment, and improve the therapeutic outcomes of hyperthermia and chemotherapy.

1. Introduction

Precision medicine in cancer treatment requires accurate diagnosis before initiating any treatment. Traditionally, this is done through the use of separate agents for diagnosis and therapy. An emerging – and potentially more powerful – approach is to apply theranostics, which deliver therapeutic and diagnostic imaging agents simultaneously within a single formulation. These have the potential to avoid undesirable differences in biodistribution and selectivity that may arise with distinct imaging and therapeutic agents [1, 2]. Theranostics aim to simultaneously image and monitor disease progression, delivery kinetics, and therapeutic outcomes, with the ultimate objective of tuning the therapy and dose with heretofore unobtainable control [3, 4]. One attractive strategy to achieve this goal is to develop stimuli-

driven “turn on” theranostics [5-7]. Multi-functional compositions of this type would enable selective delivery of therapeutic/diagnostic agents to a tumor site while simultaneously generating unique signals in response to internal cancer-associated stimuli (*e.g.* pH) or external stimuli (such as temperature or ultrasound) [5, 8-10].

Polymers which process a volume phase transition at a certain temperature (the critical point) are thermally responsive. This transition leads to a reversible and sudden transformation in solvation state [11]. Thermo-responsive systems can be spatially and temporally responsive to temperature, and thus are promising as theranostics since a number of *in vivo* temperature-regulating techniques suitable for patient treatments in a clinical setting have been developed, such as near infrared light, microwaves and ultrasound [12, 13]. The solubility of a polymer characterized with a lower critical solution temperature (LCST) decreases upon heating [14], while that of polymers having an upper critical solution temperature (UCST) increases upon heating. A variety of thermo-responsive systems based on LCST polymers have been reported as turn-on carriers for chemotherapy, and have displayed advantages including reducing dosage and side effects, and improving therapeutic outcomes *in vivo* [1-4]. However, UCST polymers have been much less investigated. Compared to LCST systems, they are expected to be more efficient in response to temperature changes, because the internal drug diffusion rate increases at higher temperature (when a UCST polymer becomes soluble) [17]. Since tumor cells are more sensitive to thermal treatment than normal cells, hyperthermia-triggered delivery platforms are particularly favourable in anticancer therapy, permitting combined effects of chemotherapy and hyperthermia induced apoptosis [18].

The nano-in-micro strategy, in which nanoscale agents are encapsulated in functional microspheres, seems to be promising for drug delivery. It is a facile way to combine benefits of both nano and micro-scale, inorganic and organic materials, and hence to obtain multi-functional platforms with improved bioavailability and therapeutic efficacy. For example, Wang *et al.* prepared nano-in-micro hydrogel capsules that can protect extracellular epidermal growth factor (EGF) from degradation and allow a sustained and localized release [19]. In an *in vivo* murine model it was shown that the microcapsules can significantly promote the proliferation of mesenchymal stem cells and thus facilitate tissue regeneration compared to with a control nanoparticle formulation loaded with EGF [19].

There exist a range of nanoscale carriers which could be incorporated into microcapsules. Of these, layered double hydroxides (LDHs) stand out because of their 2D structure, with high specific surface area, and ion exchange properties [20, 21]. LDHs generally have low toxicity and high cellular permeability, making them attractive platforms for theranostic purposes. As drug carriers, they can improve the solubilization and dissolution of hydrophobic molecules,

and protect and deliver fragile biomolecules like DNA/proteins *in vivo* [22, 23]. As diagnostic agents, LDHs have been developed for magnetic resonance imaging (MRI), computed tomography (CT), photoacoustic tomography or fluorescence imaging [24].

MTX is an antimetabolite and antifolate agent which has been clinically applied as an anticancer drug and for autoimmune disorders. Due to its high hydrophobicity and low permeability, MTX is classified into class IV of the biopharmaceutical classification (BCS) system. 5-fluorouracil (5FU) is a pyrimidine antimetabolite used to treat a number of cancers. The clinical use of both MTX and 5FU is limited by factors such as low bioavailability [25, 26], narrow therapeutic window [27] and high risks of toxicity [27, 28]. To overcome these challenges, a variety of approaches have been explored, including entrapment in a polymer matrix to obtain controlled delivery [29, 30].

Here, we designed and prepared nano-in-micro thermo-responsive microspheres as controlled delivery and theranostic systems to treat cancer as shown in Scheme 1. Firstly, LDH nanosheets were synthesized and subsequently loaded with a chemotherapeutic agent, either methotrexate (MTX) or 5FU. The drug-loaded nanocomposites were then co-encapsulated with superparamagnetic iron oxide nanoparticles (SPIONs, MRI contrast agents) into poly(acrylamide-co-acrylonitrile), a UCST microparticles *via* spray drying. The microparticles were fully characterised, and their drug release and proton relaxivities investigated in detail.

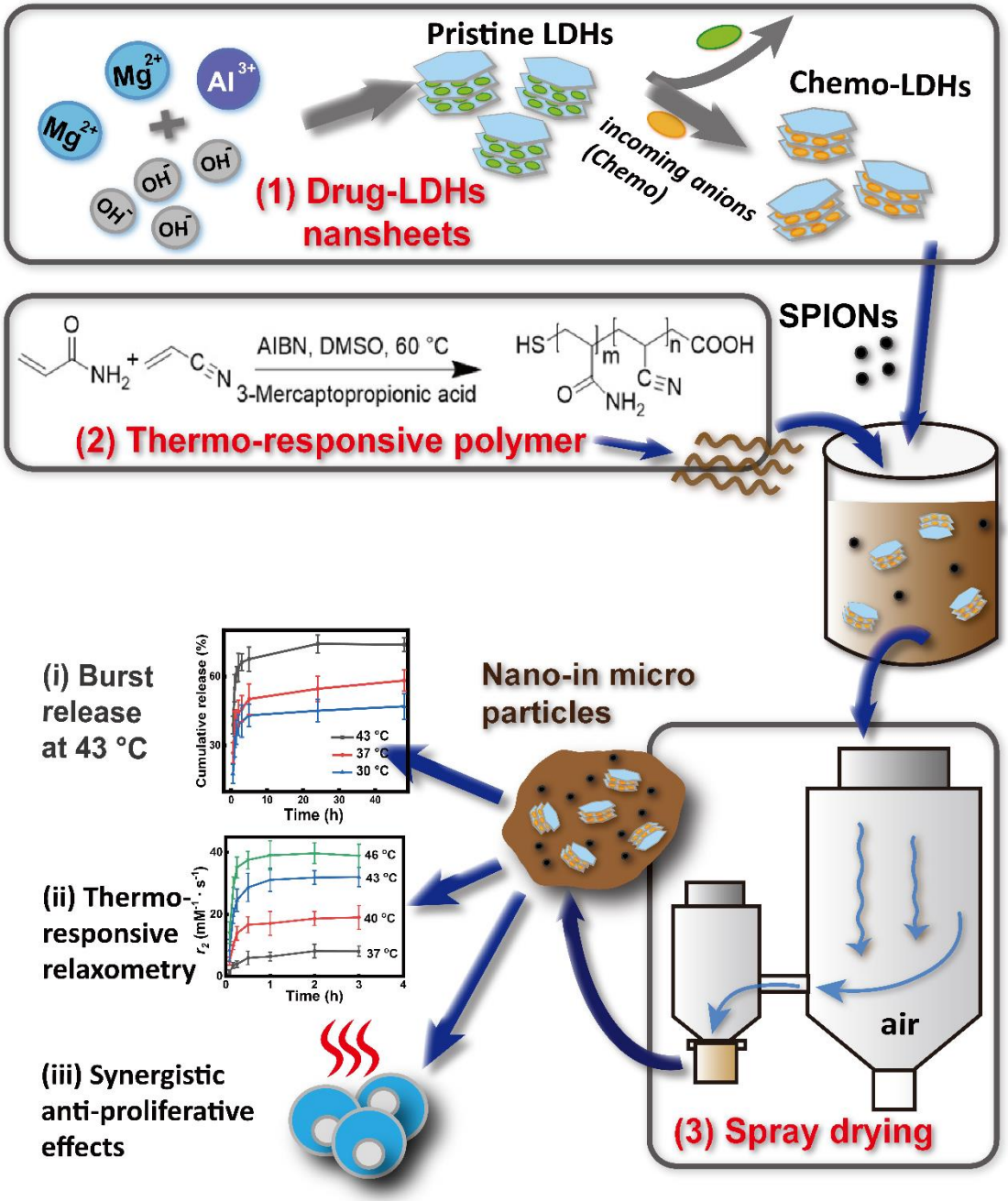

Scheme 1. Illustration of our thermal responsive nano-in-micro particles for MRI-guided chemotherapy

2. Materials and methods

2.1. Materials

Sodium hydroxide was purchased from Fisher Scientific Ltd. Sodium chloride, dimethylformamide (DMF), dimethyl sulfoxide (DMSO), acetone, anhydrous ethanol,

polyvinylpyrrolidone (PVP; 40 kDa), xanthan gum, $FeCl_3 \cdot 6H_2O$, $FeCl_2 \cdot 4H_2O$, $AlCl_3 \cdot 6H_2O$, $MgCl_2 \cdot 6H_2O$, 5-fluorouracil (5FU), crystal violet, 3-mercaptopropionic acid, azodiisobutyronitrile, acrylamide and acrylonitronile were sourced from Sigma-Aldrich. Methotrexate (MTX) was obtained from Generon. Dulbecco's modified Eagle with high glucose (DMEM-HG) was purchased from Gibco. Penicillin-streptomycin (1 % v/v), L-glutamine (1 % v/v) solutions and non-essential amino acid solution (1 % v/v) were obtained from Life Technologies.

2.2. Synthesis of PVP stabilized SPIONs

$FeCl_3 \cdot 6H_2O$ (6.5 g, 0.024 mol) and $FeCl_2 \cdot 4H_2O$ (2.48 g, 0.012 mol) were dissolved in 25 mL of deoxygenated ultrapure water. This solution was added dropwise into 250 mL of an aqueous NaOH solution (0.5 M) at 40 °C, and stirred for 1 h at this temperature. The resultant SPIONs were washed by centrifugation with deionized (DI) water until the supernatant was pH neutral, and the resultant black precipitate dried under vacuum. For PVP stabilisation, SPIONs (100 mL, 10 mg/mL in water) were mixed with 2 mL of an aqueous PVP solution (25.6 g/L, 0.64 mM), and the suspension was shaken (100 rpm) at room temperature. After 24 h, the suspension was mixed with 500 mL of aqueous acetone (H_2O/acetone, 1:10 v/v) and centrifuged at 13,200 rpm for 20 min. The supernatant was removed, and the resultant black precipitate washed with ethanol and dried in an oven at 50 °C for 24 h.

2.3. Synthesis of thermo-responsive polymer (TRP)

Poly(acrylamide-co-acrylonitrile) (P(AAm-co-AN)) was synthesised as follows. Acrylamide (2.88 g, 40.5 mmol), acrylonitrile (532 mg, 9.5 mmol), and azobisisobutyronitrile (39.2 mg, 0.24 mmol) were dissolved into 50 mL of DMSO, then bubbled with N_2 for 30 min to remove the oxygen in the solution. The mixture was reacted at 60 °C for 3 h under stirring at 50 rpm. 1 mL of a solution of 3-mercaptopropionic acid (42.5 mg, 0.4 mmol) in DMSO was then added into the solution. After 1 h, the reaction was ended by cooling in an ice bath and the polymer was precipitated in methanol and dried under vacuum.

2.4. Preparation of layered double hydroxides loaded with MTX/5FU (LDH)

The reaction protocol used was based on [31]. In a typical procedure, a salt solution (10 mL) containing $MgCl_2 \cdot 6H_2O$ (0.6 M, 1.22 g) and $AlCl_3 \cdot 6H_2O$ (0.2 M, 0.48 g) was quickly added into an aqueous NaOH solution (40 mL, 0.4 M, 0.64 g) while stirring vigorously. After stirring for 20 min, the fresh Mg_3Al-LDH slurry was collected *via* centrifugation (9000 rpm, 20 min), washed twice with 20 ml of deionized water, and re-suspended in deionized water (40 mL). Next, the slurry was heated at 100 °C for 6 hours in a 50 mL Telfon-lined stainless steel autoclave, followed by product recovery through centrifugation and washing with deionized

water until the supernatant pH was close to 7. The resultant LDH was dried under vacuum. For drug loading, 400 mg of the LDH was dispersed in an aqueous solution (20 mL) containing MTX (0.06 mmol, 455 mg) or 5FU (0.1 mmol, 390 mg) at pH 9.5. After stirring at 40 °C for 48 hours, the product was washed with DI water through centrifugation. After a final wash with acetone, the MTX or 5FU loaded Mg_3Al-LDH (LDH-MTX, LDH-5FU) was dried at 40 °C for 48 hours in an oven.

2.5. Preparation of thermo-responsive microparticles

Spray drying was performed using a mini spray dryer (Buchi B-290, Laboratory-Technik Ltd) with a closed loop. 1.0 g of TRP was firstly dissolved in 100 mL of 70 °C water containing free drug, LDH intercalates and/or SPIONs (Table 1). The spray nozzle tip diameter was 0.7 mm. The inlet air temperature was 120 °C and the outlet air temperature 80 °C. The liquid feed rate to the dryer was 20 mL/min, and the flow of drying gas approximately 5 m^3/h. Experiments were performed under constant process conditions. After letting the equipment cool down to below 60 °C, the dry powder was collected from the particle chamber.

Table 1 The compositions of different the formulations

Formulation	Chemotherapeutic (w/w)[a]	PVP-SPIONs (w/w)[b]
TRP- M	-	-
TRP- LDH	18 % LDH	-
TRP-5FU	6 % 5FU	12%
TRP-MTX	6 % MTX	12%
TRP-LDH-5FU	18 % 5FU-LDH	12%
TRP-LDH-MTX	18 % MTX-LDH	12%

a: the weight ratio of chemotherapeutic to TRP; b: the weight ratio of PVP-SPIONs to TRP

2.6. Polymer characterization

Gel permeation chromatography (GPC) was performed using a Shimadzu Prominence system fitted with a differential refractive index detector. The system was equipped with 2 x PL aquagel-OH columns (300 x 7.5 mm) and a PL aquagel 5 µm guard column. The eluent used was 0.1 M $NaNO_3$ (aq), set to a flow rate of 1 ml min^{-1} with the column oven at 55 °C. Polyethylene glycol standards (Agilent EasyVials) were used for calibration. Samples were prepared by dissolving the TRP in 0.1 M $NaNO_3$ (aq) and heating to 75 °C. 20 µL was then injected onto the column. Experimental molar mass (Mn) and dispersity (Đ) values were determined using the Shimadzu GPC software. Infrared (IR) analysis was carried out with a Brukcer Alpha I spectrometer with a ZnSe ATR crystal over the range 450-4000 cm^{-1}. Nuclear magnetic resonance (NMR) experiments were performed on a Bruker Avance 400 MHz spectrometer, with DMSO-d6 as the solvent.

2.7. Determination of upper critical point temperature (UCST)

The UCST of the TRP was determined using a UV−Vis spectrophotometer (Cary 60 instrument, Agilent) with 1 wt% phosphate-buffered saline polymer solutions (pH 7.4), by measuring absorption at 670 nm over the temperature range of 20−60 °C. The experiments were carried out with 3 heating/cooling cycle using a water bath (temperature ramp of 2 °C/min) and the transmittance was recorded every 5 seconds. The LCST was identified as the temperature at which the absorption of the sample was 50% of the maximum value.

2.8. Microscopy

The morphology of the particles was analysed with a field emission scanning electron microscope (FEI Quanta 200F) connected to a secondary electron detector (Everheart-Thornley Detector-ETD). Samples were coated with a 20 nm gold sputter (using a Quorum Q150T coater) before measurement. The size distribution of the particles was determined from the SEM micrographs by measuring them at > 100 points, with the aid of the ImageJ software (version 1.52s, National Institutes of Health). Data are reported as mean ± S.D. Energy dispersive X-ray spectroscopy (EDX) was carried out using a Carl Zeiss EVO 25 SEM with an Oxford Instruments X-max 80 EDS detector. The accelerating voltage was 20 kV, with a working distance of 8.5 mm. The Oxford Instruments Aztec 5.0 software was used to collect EDX data.

TEM images were obtained on a JEOL JEM-1200 microscope operated at 120 kV with a beam current of *ca.* 80 mA. A Gatan Orius 11-megapixel camera was used to take images. TEM samples were prepared by depositing a drop of aqueous LDH suspension on a formvar-coated 300-mesh copper grid, and then drying the grids in an oven (45 °C). Average particle size was measured with the ImageJ software (version 1.52s, National Institutes of Health).

2.9. Physicochemical properties

A MiniFlex 600 diffractometer (Rigaku) supplied with Cu-Kα radiation was used to collect X-ray diffraction (XRD) patterns (λ = 0.15418 nm, 40 kV, 15 mA). Patterns were recorded over the 2θ range from 3 to 70 ° (step = 0.01°). Thermogravimetric analysis was undertaken on a Discovery instrument (TA Instruments, Waters LLC). Ca. 3 mg of each sample was loaded into an aluminium pan and heated from 40 to 500 °C at 10 °C/min under a nitrogen flow of 25 mL/min. Data were recorded using the Trios software and analysed with TA Universal Analysis. Differential scanning calorimetry (DSC) data were obtained with a Q2000 DSC (TA Instruments, Waters LLC). A small amount of sample (approximately 3 mg) was loaded in a non-hermetically sealed aluminium pan (T130425, TA instruments) and DSC experiments carried out from 40 to 126 °C, with a temperature ramp of 10 °C/min and nitrogen purge of 25 mL/min. DSC data were recorded with the TA Advantage software package and analysed using TA Universal Analysis. X-ray photoelectron spectroscopy (XPS) measurements were

performed on an Axis Supra+ system (Kratos) with an Al Kα X-ray source (15 kV, 10 mA). FTIR analysis was performed with a Spectrum 100 instrument (PerkinElmer) over the range 650-4000 cm^{-1} at a resolution of 1 cm^{-1}. Hydrodynamic particle size and zeta potential measurements were obtained on stable aqueous dispersions of particles using a Malvern Zetasizer Nano ZS instrument. Particle sizes are reported as the average of three measurements.

2.10. Loading capacity and encapsulation efficiency

The loading capacity (LC) of 5FU and MTX in the formulations can be calculated as the amount of entrapped drug divided by the total composite mass (Equation 1). Encapsulation efficiency (EE) is the percentage of the drug present that is successfully entrapped into the composites (Equation 2).

$$\text{Loading Capacity (LC)} = \frac{Weight\ of\ total\ entrapped\ drug}{Weight\ of\ total\ drug\ added} \qquad \textbf{Equation 1}$$

$$\text{Encapsulation efficiency (EE)} = \frac{Weight\ of\ total\ entrapped\ drug}{Weight\ of\ total\ formulation} \qquad \textbf{Equation 2}$$

To determine the LDH LC and EE, 2 mg of drug loaded LDH powder (n=5) was charged in a 10 mL volumetric flask and suspended in 5 mL of DI water. The solution was acidified with one droplet of concentrated HCl, and shaken until the LDH was fully degraded. After neutralizing with 0.2 M aqueous NaOH, the solutions were made up to 10 mL with DI water. The resultant solution was filtered through a 0.22 μm PVDF-type syringe filter before being analysed with UV spectroscopy at 262 nm for 5FU and 303 nm for MTX (Cary 100 instrument, Agilent).

To calculate the LC and EE of the drug loaded thermo-responsive formulations, 2 mg of the microparticles (n=5) was placed in a 10 mL volumetric flask and suspended in 5 mL of DI water. The resultant suspensions were heated at 50 °C until the polymer was fully dissolved. For microparticles loaded with LDH nanocomposites, 1-2 droplets of concentrated HCl were also added to fully degrade the LDH nanocomposites, and the pH then adjusted to around 7 using 0.2 M aqueous NaOH. Finally, the volume of each solution was made up to 10 mL with DI water. A PVDF-type syringe filter (0.22 μm) was used to filter the resultant solutions before they were analysed with UV spectroscopy as above.

2.11. *In vitro* drug release

20 mg of each formulation (n=3) was dispersed in 5 mL of a buffer (either pH 7.4/6.5 phosphate buffered saline (PBS), or pH 5.0 acetate buffer) and transferred into a dialysis bag (molecular weight cut-off = 3500 Da). The bag was submerged into 15 mL of the appropriate buffer and

stirred at 30, 37 or 43 °C (50 rpm) using a magnetic stirrer (IKA). 0.3 mL aliquots were withdrawn from the dissolution medium at predetermined times. To maintain a constant volume, the same amount of fresh pre-heated buffer was added to the dissolution vessel. The filtrates were centrifuged for 15 min (13,200 rpm) to remove any SPIONs or microparticle residues and then analyzed with an Agilent Cary 100 spectrophotometer. MTX and 5FU quantifications were performed at λ_{max} of 303 nm for MTX and 262 nm for 5FU, respectively. Dilutions were undertaken when necessary to bring concentrations into the linear range of the calibration curve. Experiments were performed in triplicate and the results are reported as mean ± standard deviation (S.D.).

2.12. Relaxivity Measurement

An MQC+ benchtop NMR analyser (Oxford Instruments) was used to measure transverse relaxation times (T_2) of protons at 23 MHz. The Carr-Purcell-Meiboom-Gill (CPMG) method was applied, with 4 scans per experiment.

In studies to monitor the relaxivity changes with temperature, microspheres (~ 1 mg/mL) in a 0.1 % (w/v) aqueous xanthan gum solution (phosphate-buffered saline, pH 7.4) were placed into a 10 mm-diameter NMR tube. T_2 was directly monitored at the target temperature over 3 h. All experiments were performed in triplicate and the results are reported as mean ± S.D.

To explore the relationship between relaxivity changes and drug release, a dispersion of each microsphere formulation (~ 1 mg/mL) in a 0.1 % (w/v) aqueous xanthan gum solution was placed into a 10 mm-diameter NMR tube, which was held at different temperatures. T_2 was directly monitored over 48 h. At predetermined time points, 0.3 mL of suspension was taken from the NMR tube, diluted, and filtered through a PVDF-type syringe filter (0.22 µm). To measure the drug concentration, centrifugation (13,200 rpm for 10 min) was conducted to remove the SPIONs, and the supernatant analysed on an Agilent Cary 100 spectrophotometer. All experiments were performed in triplicate and the results are reported as mean ± S.D.

In a set of experiments to predict drug release, dispersions of microparticles samples at 1 mg/mL in 0.1% w/v xanthan gum buffer (n=3) were placed into 10 mm NMR tubes. The transverse relaxation time was monitored at 43 or 37 °C for 5 h. At selected time points, 0.3 mL aliquots were taken from the NMR tube and the drug content in each aliquot quantified as above.

2.13. *In vitro* cell studies

The colorectal adenocarcinoma cell line Caco-2 (ATCC HTB-37), A549 cells (ATCC CCL-18), an adenocarcinomic human alveolar basal epithelial cell line, and human embryonic kidney cells HEK-293 (ATCC CRL-1573) were employed for *in vitro* studies. Caco-2 cells were

maintained at 37 °C, under 5 % CO_2, in DMEM-HG supplemented with penicillin-streptomycin (1 % v/v), L-glutamine (1 % v/v), and non-essential amino acid (1 % v/v) solutions and 10 % v/v heat-inactivated fetal bovine serum. A549 and HEK-293 cells were cultured in DMEM-HG supplemented with pre-heated fetal bovine serum (10% v/v), L-glutamine (1% v/v) and penicillin (1% v/v) solutions.

For viability assays, A549 or Caco-2 cells were pre-grown in 96 well plates (ThermoScientific). 1×10^4 cells in 200 µL of medium were seeded into each well and cultured for 24 h. The medium was aspirated, and 200 µL of pre-heated DMEM containing various concentrations of TRP-LDH-drug or TRP-drug microparticles was added. As controls, the raw drugs 5FU and MTX were dissolved in dimethyl sulfoxide (DMSO) and stored at 4 °C before use. 5FU and MTX were then diluted using culture media to various concentrations. The final concentration of DMSO did not exceed 0.1 v/v % in the culture medium.

Hyperthermia was induced by elevating the temperature of an incubator to 43 °C. After 60 min of exposure, cells were immediately moved back to an incubator at 37 °C and maintained for 24 h. Cell viability was determined using the PrestoBlue™ cell viability assay (ThermoFisher). Briefly, the wells were aspirated and cultures were washed with PBS, followed by addition of 20 µL of the fluorescent reagent and 180 µL of DMEM medium. After addition, the plate was incubated for 20 minutes at 37 °C and 5 % CO_2 before fluorescence was read at 560 (λ_{ex}) and 590 (λ_{em}) nm using a SpectraMax M2^e spectrophotometer (Molecular Devices). The viability of the cells was calculated using Equation 3:

$$Viability = \frac{Fluorescence\ \ of\ treated\ cells - background}{Fluorescence\ \ of\ untreated\ cells - background} \qquad \textbf{Equation 3}$$

In multi-hyperthermia cell studies, A549 or Caco-2 cells were pre-grown in 96 well plates. 1×10^4 cells in 200 µL of medium were seeded into each well and cultured for 24 h. The medium was aspirated and 200 µL of pre-heated DMEM containing TRP-LDH-MTX (at a concentration of 50 ng/mL MTX) were added. Hyperthermal treatment was induced every 24 h by elevating the temperature of an incubator to 43 °C. After 60 min of exposure, cells were immediately moved back to an incubator with temperature set at 37 °C. Cell viability was determined using the PrestoBlue™ cell viability assay (ThermoFisher) as described above. Cell viability data were compared by Student's t-tests. For the crystal violet assay, cell cultures were washed with PBS, fixed with 10 v/v % formalin for 15 min, followed by incubation with 0.1w/v % crystal violet solution for 20 min. After staining cells were carefully washed three times with PBS and imaged on an Evos XL Core light microscope (Invitrogen, Thermo Fisher Scientific).

3. Results

3.1. Synthesis of PVP-stabilized SPIONs

PVP stabilized superparamagnetic iron oxide nanoparticles (PVP-SPIONs) were prepared as MRI contrast agents following a previously reported protocol [10]. The mean size of the particles is 8.5 ± 2.7 nm (TEM; the Supplementary Information, Fig. S1A) and XRD (Fig. S1B) confirms the successful synthesis of SPIONs. The reflections at 30.2, 35.5, 43.7, 53.6, 57.1 and 62.9° can be indexed to the (022), (311), (004), (333), (115), and (044) planes of the cubic inverse spinel Fe_3O_4 (ICSD entry 77592).

3.2. Synthesis of TRP

The TRP was generated by copolymerizing acrylamide and acrylonitrile (Scheme S1) based on a previous study [32]. The FTIR spectrum of TRP (Fig. S2A) shows the presence of amide absorptions at around 1653 cm^{-1} and 1614 cm^{-1}. The characteristic peak at 2241 cm^{-1} can be identified as the stretching vibration of CN groups from acrylonitrile. The disappearance of alkenyl hydrogens with a chemical shift (δ ppm) of 5.0-6.5 in ^{1}H-NMR spectrum of TRP (400 MHz, DMSO-d_6) further confirms the polymerization of acrylonitrile and acrylamide (Fig. S2B). The characteristic peaks (δ ppm) in the ^{1}H-NMR spectrum of TRP are as follows: 1.2-1.9 (polymer backbone, -CH_2-), 2.0-2.8 (polymer backbone, -CH-$CONH_2$ and -CH-CN), 6.6-7.8 (-NH_2). The disappearance of alkenyl hydrogens (between 5.0 to 6.5) from acrylonitrile and acrylamide confirms the successful polymerization. The cloud point was determined by measuring the turbidity changes of polymer solutions with temperature, with the UCST defined as the temperature corresponding to 50% of the maximum absorption at 670 nm (with a polymer concentration of 1 wt%). The turbidity curves are shown in Fig. S3. TRP has a UCST of 32.7 °C, and is shown to have reversible behaviour in response to temperature changes, without any shift in the cloud point after three cycles of cooling and heating. Molecular weight and dispersity (*Đ*) of the synthesised copolymer were determined by GPC, and the number average M_n and weight average M_w found to be 114300 and 29700 g/mol, respectively, with *Đ* of 3.84. The average M_w is similar to the literature [32], but the M_n and *Đ* are larger, indicating the polymer synthesized here has a broader molecular weight distribution.

3.3. Preparation of MTX/5FU loaded LDH

The morphologies of the LDH-drug particles were characterized using TEM and SEM analysis (Fig. S4A-D). LDH-MTX and LDH-5FU exists as plate-like nanoparticles in both sets of TEM images. In SEM images (obtained after oven drying), plate-like structures still can be seen, though the drug-loaded LDH materials have become aggregated. Fig. S4E presents the XRD

patterns of pristine LDH, LDH-5FU and LDH-MTX, in which the reflections can be indexed to (003), (006) and (009) reflections of LDH phases. Compared to the XRD pattern of the parent LDH, the (003) and (006) reflections are broader after MTX or 5FU intercalation and shift to lower angle. The latter arises owing to the incorporation of a larger drug ion between the layers causing them to move apart, and the increase in peak broadness is indicative of increased stacking defects [33, 34]. The drug loaded LDHs displayed expanded structures with basal spacings of 10.4 Å and 20.1 Å for LDH-5FU and LDH-MTX, greater than that of the pristine LDHs (8.2 Å). These observations are all consistent with the literature [35, 36]. No XRD reflections from the pure drug can be seen in the patterns (Fig. S4F), suggesting no pure drug crystals are present.

IR spectra are shown in Fig. S4G. In the parent LDH, the stretching bands of both hydroxide and interlayer water molecule are found at approximately 3400 cm^{-1}, and a band at 1647 cm^{-1} can be ascribed to the δ-bend of water. The low intensity peak at around 1450 cm^{-1} can be attributed to the C=C stretching vibration of MTX in LDH-MTX, and the peak at 1610 cm^{-1} corresponds to the water bending mode. Further, a pair of absorption bands at 1387 and 1558 cm^{-1} may be attributed to COO^- stretching vibrations of MTX. Similarly, successful intercalation of 5FU was confirmed by IR. There are a range of additional peaks characteristic of 5FU in LDH-5FU, which arise around 1672 cm^{-1} (C=O and C=C stretches), 1586–1300 and 809 cm^{-1} (ring stretching modes) [45], and 1216 cm^{-1} (C–F vibrations) [37].

3.4. Preparation of thermo-responsive particles

Spray dying was used to fabricate thermo-responsive microspheres loading with SPIONs and LDH-5FU or LDH-MTX. Firstly, blank TRP microparticles (TRP-M) and particles loaded with LDH (TRP-LDH) were prepared, as displayed in Fig. S5. It can be observed that both sets of microparticles exist in a concave shape, with mean diameters of 1.28 ± 0.53 and 2.53 ± 1.11 μm respectively (Fig. S6A, B). The encapsulation of LDH results in an increase in particle size and a more uneven surface.

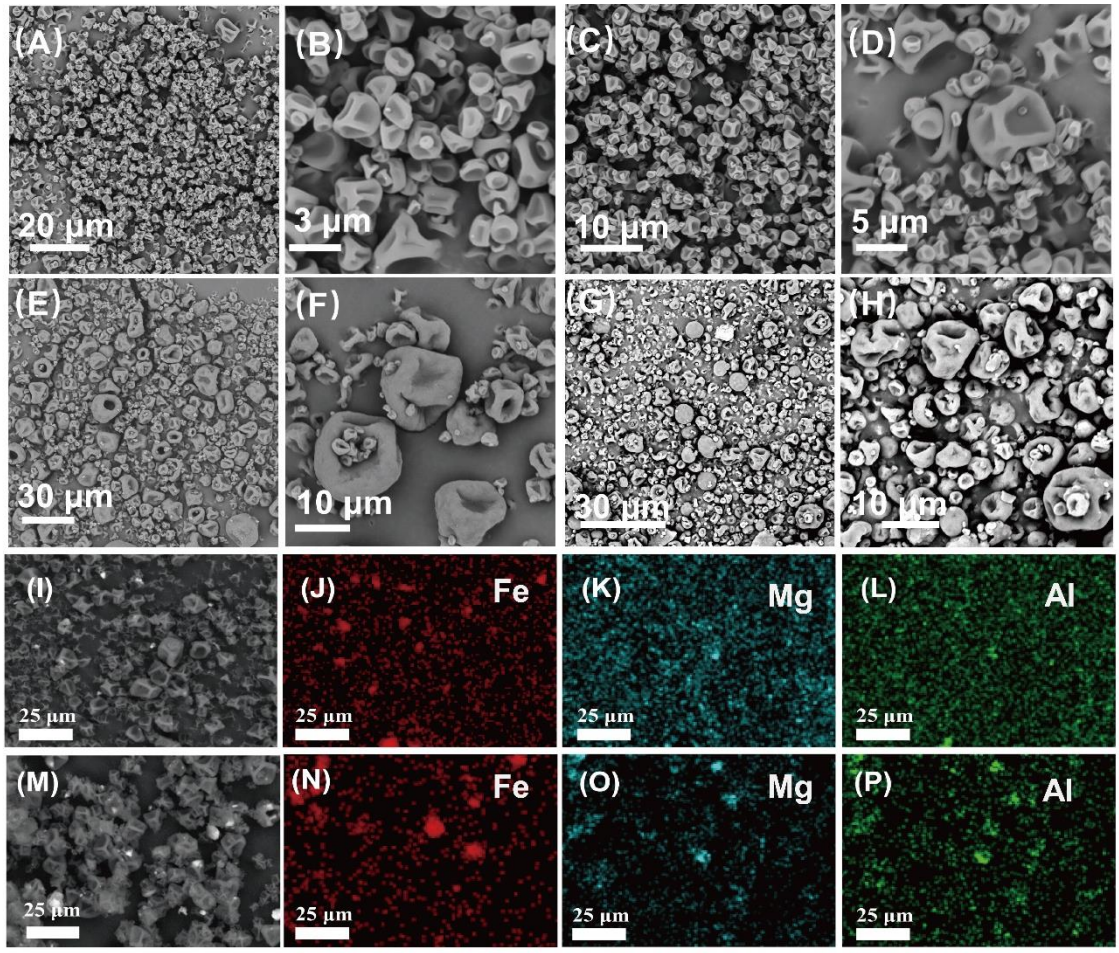

Fig. 1. SEM images of (A, B) TRP-MTX, (C, D) TRP-5FU, (E, F) TRP-LDH-MTX and (G, H) TRP-LDH-5FU. Fe, Mg, and Al elemental mapping of (I-L) TRP-LDH-MTX and (M-P) TRP-LDH-5FU.

The microparticles carrying MTX or 5FU and PVP-SPIONs (TRP-MTX or TRP-5FU) have similar morphology to TRP-M, exhibiting concave structures with relatively smooth surfaces (Fig. 1A-D). The mean sizes of TRP-MTX and TRP-5FU are 1.67 ± 0.65 μm and 1.56 ± 0.64 μm, close to that of TRP-M. As can be seen in Fig. 1E-H, microparticles carrying SPIONs and LDH-MTX or LDH-5FU are relatively larger (2.74 ± 1.48 μm for TRP-LDH-MTX, 2.83 ± 1.83 μm for TRP-LDH-5FU, Fig. S6C-F), and possess concave shapes with rough surfaces, analogous to TRP-LDH. Particles of this size are appropriate for use in inhalation drug delivery, or could be implanted in a tumor site after resection of the cancer. Elemental mapping results (Fig. 1I-P and Fig. S7) showed that Fe, Mg and Al are uniformly distributed in the particles.

The XRD profiles of TRP-5FU and TRP-MTX are given in Fig. 2A. Reflections of SPIONs are observed, and a broad peak from 15-25° is very similar to that seen in the pattern of TRP. No reflections from the raw drugs are seen in the composites. This indicates that amorphous solid dispersions have formed, as would be expected with spray drying [38, 39]. A similar broad peak (15-25°) can be found in the XRD patterns of TRP-LDH-MTX and TRP-LDH-5FU, as a

result of the presence of TRP (Fig. 2B). Reflection of SPIONs can be found superimposed on this amorphous halo, suggesting the successful encapsulation of SPIONs. Distinctive reflections of the drug loaded LDH were not observed, likely because the LDH-drug peaks have low intensity.

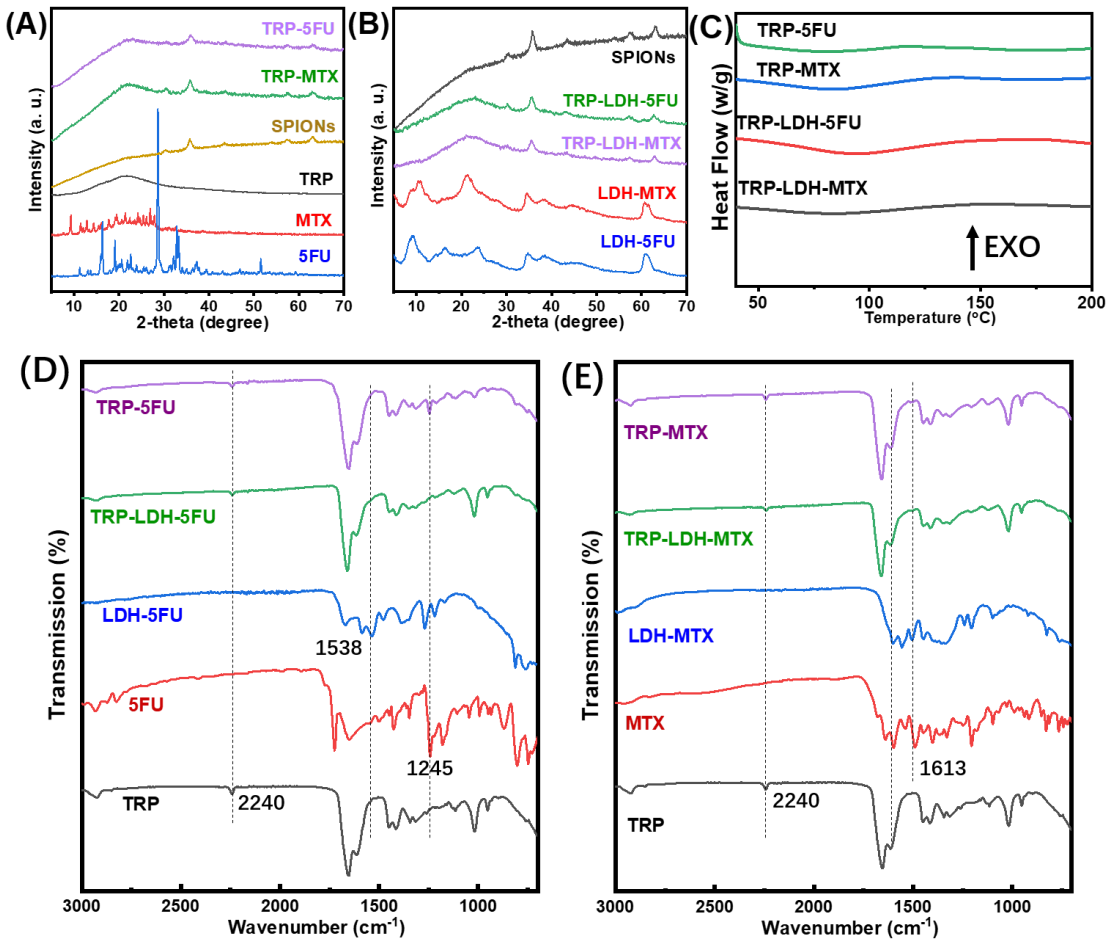

Fig. 2. (A, B) XRD patterns of the raw materials and microparticles; (C) DSC profiles, (D, E) IR spectra.

Additiona l evidence for the amorphous nature of MTX and 5FU in the TRP-drug formulations comes from their DSC profiles. A clear endotherm around 120 °C can be seen in the DSC profile of MTX (Fig. S8A), as has previously been observed in the literature [40]. No such endotherm was observed in TRP-MTX (Fig. 2C and Fig. S8A). For microparticles loaded with 5FU, the DSC profile provides little information because the melting of 5FU occurs at around 280 °C, beyond the temperature where TRP begin to decompose (Fig. S8B). A broad endotherm between 40 to 110 °C is seen in the DSC data of all microparticles, and can be attributed to the evaporation of adsorbed or absorbed water.

FTIR spectra of the formulations are given in Fig. 2D-E. The CN stretching vibrations of TRP (2240 cm^{-1}) are visible in all formulations. For LDH-loaded microparticles, the band between 1504 to 1616 cm^{-1} becomes broader, suggesting the encapsulation of drug loaded LDH. The characteristic peaks at 1245 cm^{-1} of TRP-5FU arises from C–F vibrations of 5FU, while for TRP-MTX the small band at around 1503 cm^{-1} can be attributed to the COO^- stretching vibrations of MTX.

3.5. Drug loading and release

The LC and EE data are listed in Table 2. The LC of LDH-MTX (43.5 ± 6.2 %) is higher than that of LDH-5FU (14.8 ± 1.9 %), consistent with the literature [41, 42]. Both the TRP-drug and TRP-LDH-drug microparticles displayed high encapsulation efficiency (EE), reaching more than 89.8 %.

Drug release from the microparticles was explored in PBS and acetate buffers, and at temperatures of 30, 37 and 43 °C. 37 °C is the standard physiological temperature. A warm environment of 43 °C was used to mimic the moderate temperature hyperthermia (42–45 °C) that has been utilized in clinical trials with minimal side effects [43, 44]. 30 °C (a temperature below the UCST of TRP) is not likely to be experienced physiologically except at the body exterior (the skin has a typical temperature around 32 °C [45, 46]), but was selected to give insight into the thermo-associated behavior of the formulations. Three pHs, 5.0, 6.5 and 7.4 were explored. pH 6.5 was selected to mimic the slightly acidic pH of the tumor microenvironment, while pH 7.4 represents normal physiological conditions. pH 5.0 was chosen to mimic a late endosomal/lysosomal environment [47-49].

Table 2 LC and EE of the different formulations.

Materials	LC (%)	EE (%)
LDH-MTX	43.5 ± 6.2	-
LDH-5FU	14.8 ± 1.9	-
TRP-LDH-5FU	1.94 ± 0.09	95.6 ± 4.34
TRP-LDH-MTX	5.45 ± 0.41	90.5 ± 6.81
TRP-5FU	4.82 ± 0.44	94.9 ± 8.66
TRP-MTX	4.56 ± 0.53	89.8 ± 10.4

(LC, loading capacity; EE, encapsulation efficiency)

The release profiles of drug loaded LDHs were first explored at 37 °C. Both LDH-MTX and LDH-5FU displayed pH-responsive release, with more release at lower pH, ending with more than 60 % or 70 % of drug freed from LDH-MTX or LDH-5FU after 45 h, respectively (Fig. S9A-B). Data for TRP-5FU and TRP-MTX are given in Fig. S9C-F. Significant burst release (> 50% in the first hour) was seen with both the TRP–drug materials, regardless of pH and temperature. This presumably arises due to the molecular distribution of drug in the polymer carrier and the high surface area of the microparticles. Thus, even when the polymer is

insoluble the drug can diffuse out of the matrix into solution. Both TRP-MTX and TRP-5FU display accelerated drug release at higher temperatures. There is no clear pH response noted, though there appears to be a slight tendency for more rapid release at lower pHs.

The drug release profiles over 120 h from the TRP-LDH-drug composites are included in Fig. 3, with an insert panel reflecting an enlargement of the first 7 h. At 43 °C, a burst release of up to 60% can be observed in the first 2 hours, and the TRP-LDH-drug composites display very rapid release as a result of polymer matrix dissolution. The systems at 30 or 37 °C all present a rapid release in the initial period (0-3 h), followed by very slow release (3-120 h). The first stage of release is mainly driven by the presence of some LDH–drug particles at the surface of the microparticles [50]. The second stage of release arises due to the drug escaping from LDH particles at the inside of the polymer matrix. Compared to the TRP-drug systems, the TRP-LDH-drug composites can reduce the initial burst of drug release and demonstrate a more markedly temperature responsive profile. Further comparison of the release data of TRP-LDH-drug at different pHs (37 °C) demonstrates there is some pH-responsiveness with these formulations too, with more rapid release at lower pH values in the case of 5FU (Fig. 3C). In contrast, MTX release is slowest at low pH (Fig. 3F). These findings can be attributed to a combination of the pH sensitive properties of LDHs, which are able to partially dissolve at lower pHs [51, 52], and the relative solubilities of the drug molecules. 5FU is amphoteric and has high solubility at all pH values studied, and thus the release properties are expected to be a result of the LDH degrading at lower pH. MTX is an acidic drug containing two carboxylic acid units, with pKa values of 4.8 and 5.5. The degree of MTX ionisation in solution, and thus the solubility, will be higher at elevated pH. As a result, MTX release is fastest at pH 7.4. Overall, the results showed that the nano-in-micro formulations prolong drug release and significantly enhance the responsiveness to temperature.

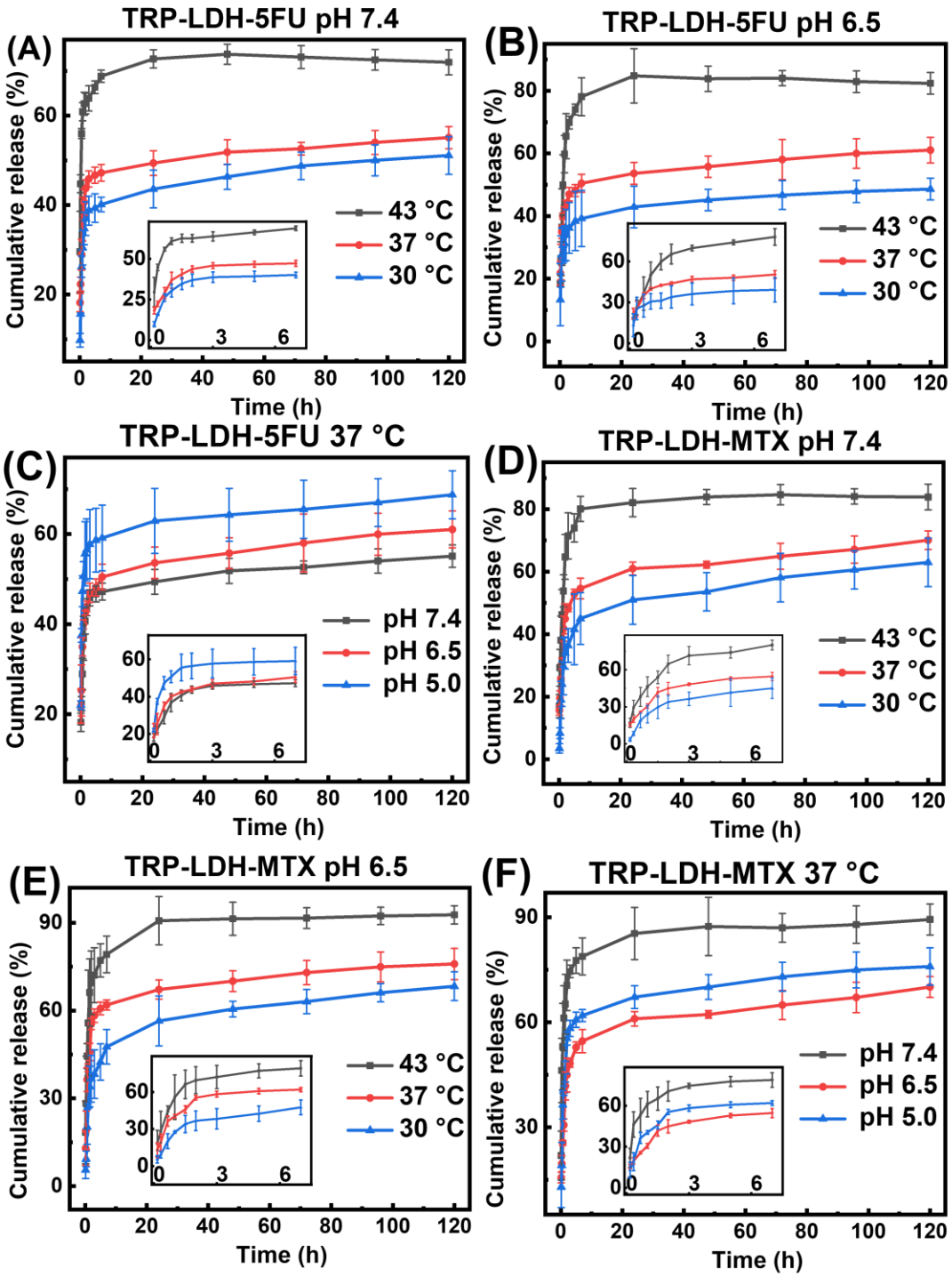

Fig. 3. Cumulative release of 5FU from TRP-LDH-5FU in pH (A) 7.4 or (B) 6.5 PBS at different temperatures over 120 h; (C) a comparison of 5FU release at different pHs and 37 °C; cumulative release of MTX from TRP-LDH-MTX in pH (D) 7.4 or (E) 6.5 PBS at different temperature over 120 h; (F) a comparison of MTX release at different pHs and 37 °C. Data obtained by UV-vis analysis and given from three independent experiments as mean ± S.D.

The release profile is controlled by several factors: the diffusion behavior of the replacement ions/molecules entering the polymer/LDH matrix, the ion-exchange reaction time, and the

diffusion of drug ions out of the microparticles. This process is rapid at 43 °C because the polymer is hydrophilic and soluble at this temperature; thus, water quickly diffuses into the polymeric matrix. At lower temperatures, this diffusion process is very slow and release extending for several days is observed. At 37 or 30 °C, TRP microparticles give an almost constant rate of release between 24–120 h, and fitting zero-order kinetics to the data over this period gives good fits (R^2 = 0.94-0.99), as displayed in Figs. S10 and S11 [50]. While at 43, the zero-model doesn't give good fits since TRP were soluble and drug quickly free into mediums. The results suggest the TRP-LDH-drug composites are capable of providing sustained delivery of chemotherapeutics for cancer treatment. Hence, they provide two delivery options: fast release can be triggered to arrest rapidly growing tumors by raising the surrounding tissue temperature *via* the application of an external heat source, and without this stimulus the formulations act as slow release matrices to maintain the drug concentration at a therapeutic level over a prolonged period of time.

To understand better the mechanism of drug release, the Peppas model (Equation 4) was fitted to the first 60% of the release data [53]. M_t/M_∞ (Q_t) represents the extent of drug release, k is a rate constant, and m gives information related to the mechanism of release.

$$\boldsymbol{M_t/M_\infty = ke^m} \qquad \textbf{Equation 4}$$

The results are summarized in Figs. S12-15 and Table S1. The fits are generally good with (R^2 > 0.95), although some of those for TRP-LDH-5FU (pH 6.5, 30 °C, pH 6.5, 37 °C and pH 5.0, 30 °C) and TRP-LDH-MTX (pH 5.0, 30 °C) are relatively poor. Release data for the TRP-drug composites commonly display poorer correlation with the Peppas model, with R^2 in the range of 0.75-0.97. The Peppas exponents are in the range 0.45 to 0.89, suggesting drug release occurs through a combination of matrix swelling and drug diffusion.

3.6. Proton relaxivity

T_2 relaxation behaviour of the TRP-LDH-drug particles was investigated at three different temperatures (30, 37 and 43 °C). The drug release profile was monitored as a function of incubation time to elucidate any relationship between the drug release and proton relaxation changes.

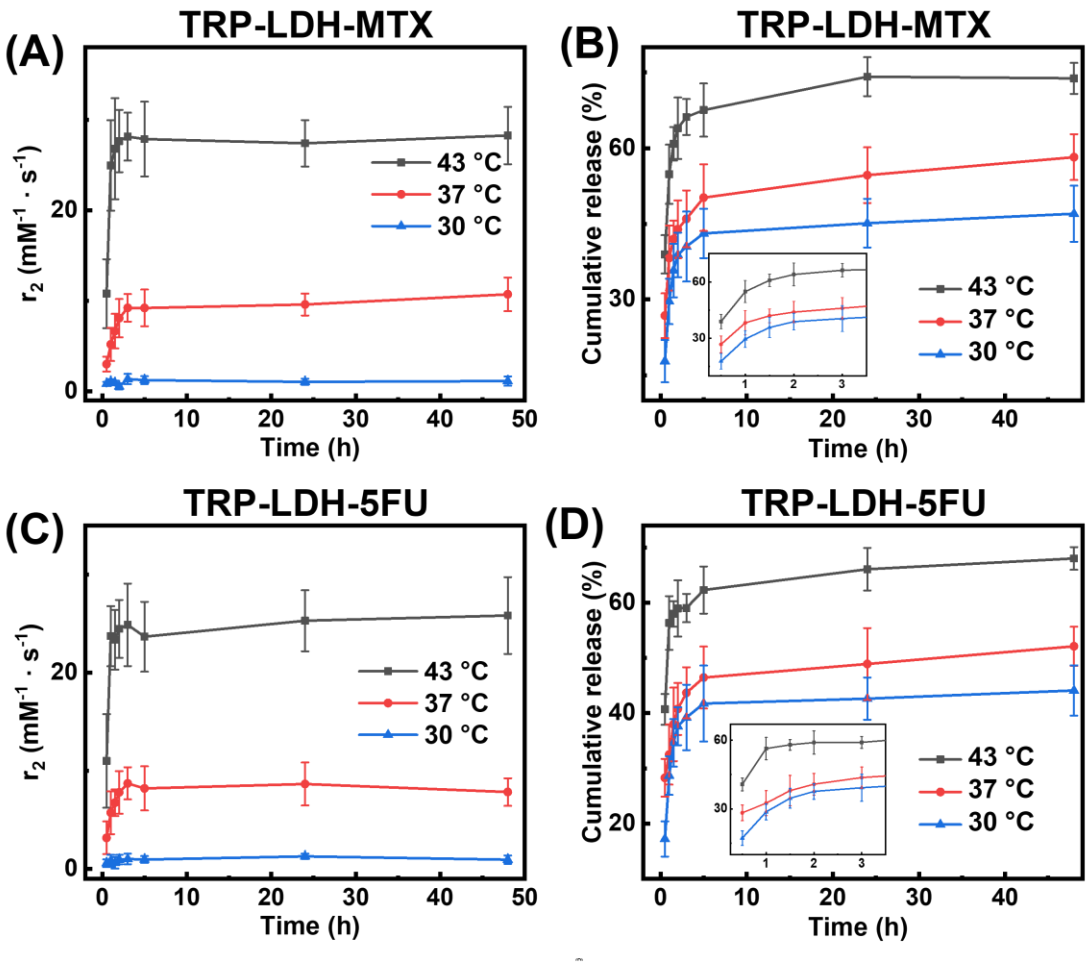

Fig. 4. The relaxivity and corresponding drug release profile of (A-B) TRP-LDH-MTX and (C-D) TRP-LDH-5FU. (A, C) show transverse relaxivity and (B, D) drug release over 48 h, with an enlargement of first 3 h. Data given from three independent experiments as mean ± S.D.

Table 3 DLS data of TRP-LDH-5FU at different temperatures (n=3).

Temperature (°C)	Z-average (nm)	PDI	Zeta-potential (mV)
46.0	204 ± 16	0.28 ± 0.06	1.15 ± 0.04
43.0	232 ± 8	0.38 ± 0.05	1.30 ± 0.24
40.0	377 ± 8	0.61 ± 0.05	1.47 ± 0.04
37.0	1216 ± 90	0.42 ± 0.19	1.80 ± 0.23
35.0	2224 ± 36	0.24 ± 0.36	2.25 ± 0.04
30.0	8876 ± 801	1	-

The relaxivity profiles of the LDH-containing microparticles as a function of incubation time are shown in Fig. 4. When microparticles were immersed in the mediums, the initial relaxivity r_2 value (measured after 10 min suspension) was low. The r_2 values increased with time as the microparticles remained suspended in mediums as shown in Fig. 4A, C. This was due to the dynamic process of matrix dissolution/swelling as reported our previous study [10]. The

dynamic dissolution/swelling process enables water molecules access to the SPIONs, boosting diffusive water access and hence enhancing their relaxation rates and thus relaxivities. Thus, instead of measuring a single r_2 value, the r_2 relaxivity was monitored as a function of time during incubation at different temperature. The resultant r_2 profiles can help to determine whether MRI signal could be utilised as a mechanism of monitoring microparticles dissolution/swelling, and hence drug release and temperature change.

As given in Fig.4, r_2 values remained very low over 48 h (~ 1 $mM^{-1} \cdot s^{-1}$) at 30 °C. This is because the TRP is hydrophobic and insoluble in medium at this temperature, thus the MRI-active SPIONs stayed inside the formulations, preventing their effective magnetic interaction with diffusive water protons. The drug release was rapid in the first 3 hours at all temperature (**Figure 4.B, D**), as was seen in the previous dissolution tests.

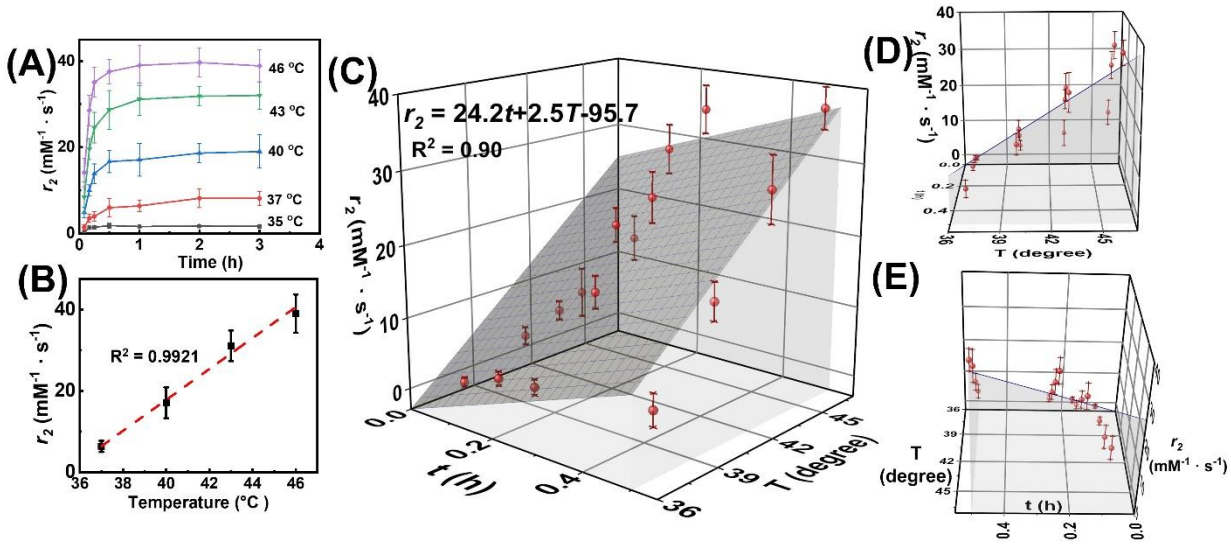

Fig. 5. (A) The r_2 vs time profile of TRP-LDH-5FU at different temperatures; (B) the relationship between temperature and relaxation behaviour (r_2) after 1 hour of TRP-LDH-5FU; (C) results of binary linear regression on r_2 data of TRP-LDH-5FU over the first 30 min vs time (*t*) & temperature (*T*), and view of (D) time-r_2 *or (E)* temperature-r_2 panels.

The overall relaxivity at 43 °C is higher than at 37 °C, and the r_2 vs time profile is clearly thermo-responsive. This is due to dissolution/swelling and concomitant water access boosting relaxation rates, as previous described. To further explore this, r_2 of TRP-LDH-5FU in PBS buffer (pH 7.4) was explored as a function of incubation time at a range of further temperatures (35 - 46 °C). The results are given in Fig. 5A. r_2 values rapidly increased after less than 1 hour of incubation at all temperature except 35 °C, and the profiles are clearly thermo-responsive around physiological temperatures. This can be related the variation in hydrophilicity of TRP with temperature. As revealed by DLS data on TRP-LDH-5FU microparticles after 2 h incubation (Table 3), the polymer containing SPIONs undergo a rapid coil-to-globule transition

with a decreasing temperature around their UCST, with reduced diffusive water access meaning lessened relaxivitiy enhancement, whereas the water miscibility of TRP above the UCST results in a higher surface area to volume ratio and a greater surface area for SPION-water interactions [54]. Zeta potential data are also provided in Table 3. They are found to be close to zero in all temperature. Plotting the r_2 values after 1 hour of incubation (where r_2 reaches a plateau and becomes stable) against temperature, shows a clear linear correlation, which suggests the potential of the formulations to allow *in situ* monitoring of the temperature by MRI (Fig. 5B).

Furthermore, it can be observed that r_2 undergoes a dramatic increase in first 30 min in the relaxivity curves between 37–46 °C. We hypothesized that the relaxivity value over this initial period is closely dependent on both temperature and the incubation time. To test this, a binary linear regression was conducted using temperature and incubation time as independent variables, and r_2 data in first 30 min as the dependent variable. Mathematical equations could be constructed with a R^2 of 0.90 (Fig. 5C-F), indicating a good linear correlation. Hence, this formulation can provide a potential strategy utilizing the dynamic structural transformation of the TRP at temperatures beyond the UCST to monitor in real-time the temperature by MRI. Since high temperatures in hyperthermia can harm healthy surrounding tissues, it is desirable to temporally and spatially monitor the temperature during treatment.

The relationship between drug release profiles and relaxivity at 43 or 37 °C was explored, and plots of cumulative drug release vs r_2 were constructed over 300 min. Here we normalised the r_2 values in each system by calculating r_{2_t}/r_{2_max} to establish predictive equations at 43 and 37 °C. The data at 30 °C were not analysed because r_2 values at that pH remained low over 48 h. The r_{2_max} represents the maximum relaxivity value possible with the formulations, which manifests in our experiments as the relaxivity after 48 h. In the clinic, the r_{2_t} can be regarded as the local MR signal intensity at a certain time point, and r_{2_max} is the theoretical maximum MR signal intensity, a constant related to the specific formulation and dose. Fig. S16 shows that plots of drug release vs r_{2_t}/r_{2_48} reveal direct proportionality ($R^2 > 0.90$), and the best fit equations are given in Table S2.

To further validate the predictive ability of the r_2 data, the equations correlating release with relaxation behaviour were applied to predict drug release in a new series of experiments. Relaxation behaviour changes were determined at 1 mg/mL (n=3) and used to predict the extent of drug release. The latter was then measured by UV-vis spectroscopy.

$$\boldsymbol{F_1 = \left(\frac{\sum|R_t - T_t|}{\sum R_t}\right) \times 100} \qquad \textbf{Equation 3}$$

$$F_2 = 50 \times \log\left\{100 \times \left[1 + \frac{\sum(R_t - T_t)^2}{n}\right]^{-0.5}\right\} \qquad \textbf{Equation 4}$$

Fig. S17 gives the predicted and experimental release curves. The 'similarity' of predicted and experimental curves is further analysed by two fit factors F_1 (the difference factor) and F_2 (the similarity factor) (Equations 3 and 4), which were applied to statistically compare the experimental dissolution profile and that calculated based on relaxivity [55]. R_t and T_t represents the percentage of active pharmaceutical ingredient released from reference and test samples at time point t, respectively, and n is the number of time points. Two dissolution profiles are regarded to be "same" or "equivalent" when F_1 is less than 15 and F_2 is greater than 50 [56]. As detailed in Table S3, all the predicted values lie in the range of "equivalent". Both microparticles at 43 °C displayed higher similarity (lower F_1 and higher F_2) compared to curves at 37 °C, which is consistent with the results in Fig. S17. For both microparticles at 43 °C, the predicted and experimental curves generally are similar in shape, while at 37 °C, the predicted curves are different from the experimental data. Hence, our results suggest that the fitting equations built on r_2 profile could be generally reliable to predict the release at 43 °C.

3.7. *In vitro* cell studies

Firstly, HEK-239 cell line was employed to evaluate the safety of the formulations for biomedical applications. Cell viability was evaluated via PrestoBlue™, a cell metabolic activity assay. After a 24 h incubation at 37 °C TRP-M does not appear to be significantly cytotoxic at all concentrations (cell viability > 90 %) as shown in Fig. S18A. The effect of the drug loaded microparticles on HEK-293 cells was also explored (Fig. S18B,C). Here, cytotoxicity was tested using two concentrations of particles. All the drug loaded microparticles display statistically significant cytotoxicity (Fig. S18B,C), with greater toxicity at higher concentrations. This cell death arises from the loaded cytotoxic agents. The TRP-LDH-drug formulations result in higher viability than the TRP-drug systems, as a result of slower drug release from the former.

Hyperthermia has been used clinically as an adjuvant to chemo- or radiotherapy [57, 58] since it can enhance local perfusion of drugs, sensitise cancer cells to cytotoxic agents, suppress DNA repair, and improve tissue oxygenation [59, 60]. However, using temperatures over 50 °C can be harmful to healthy surrounding tissues, while the damage induced by mild heating stress (42-45 °C) tends to be repaired by a cancer cell's intrinsic thermoresistance system. A combination of mild hyperthermia and chemotherapy can dramatically enhance treatment efficacy. Here cell studies were conducted to explore the anti-cancer effect of our formulations, combining chemotherapy and mild hyperthermia (MHT). Given the fact that the local hyperthermia therapy is generally conducted for 20–60 min at a temperature between 42–

45 °C [61-63], cells treated with TRP-drug or TRP-LDH-drug were first incubated at 43 °C for 1 h before moving to physiological temperature (37 °C).

The cytotoxicity of the TRP-M microparticles to Caco-2 or A549 cells was explored at a range of concentrations after 24 h incubation at 37 °C, with or without 1 h hyperthermia (43 °C). The data showed (Fig. S19) that viability treated at 37 °C is always high, indicating that the microparticles are biocompatible and do not induce cytotoxicity to either cell type (viability > 95 %). Viability of both cell lines decreased when MHT conducted in isolation ($p<0.05$).

To explore the synergistic effect of hyperthermia and chemotherapy, TRP-LDH-drug, TRP-drug or free drug in solution (at a concentration equal to 100 % release) were applied to both cells exposed to hyperthermal conditions (43 °C, 60 min) (Fig. S20). Chemotherapy without any heat treatment induced cell death in both Caco-2 and A549 cultures treated with 5FU or MTX (see Fig. S20A, B, E, F). A significant decrease in cell viability can be seen upon heat exposure except for A549 cells treated with 5FU. A similar decrease can be found in cells treated with TRP-drug microparticles (Fig. S20C, D, G, H).

Similar to the drugs and TRP-drug formulations, the TRP-LDH-5FU and TRP-LDH-MTX formulations are toxic to the cells (Fig. 6A-D). In most cases, the viability of both cell lines decreased by a greater extent after exposure to high temperature ($p< 0.01$-0.001) compared to the results found with the drugs or TRP-drug formulations with MHT. Visual observation showed a decrease in the cell numbers (Fig. 7), confirming the anti-proliferative effect of the chemotherapy and hyperthermia combination. With the TRP-LDH-drug materials, both cell types displayed higher viability compared to those treated with only the drug, since not all the drug was released during the *in vitro* experiments. When combined with hyperthermia, the cell death induced by TRP-LDH-drug microparticles was significantly increased.

Fig. S21 compares cell viability data for chemotherapeutic, TRP-drug and TRP-LDH-drug microparticles. At a drug concentration of 100 ng/mL, MTX and TRP-MTX displays similar anti-proliferative effects on both Caco-2 and A549 cells after 24 h incubation, 37 °C with or without MHT. This indicates that the majority of MTX loaded were released from TRP-MTX microparticles in 24 h. While for TRP-LDH-MTX, the cell viability decreased in a larger extent after MHT treatment, as an indicative of thermal-triggered MTX release. Similar results can be observed in 5FU and 5FU loaded microparticles (at a concentration of 0.5 µg/mL). The *in vitro* proliferation inhibition data further confirmed the thermo-sensitive drug release of our nano-in-micro formulations, as consistent with the previous *in vitro* dissolution test.

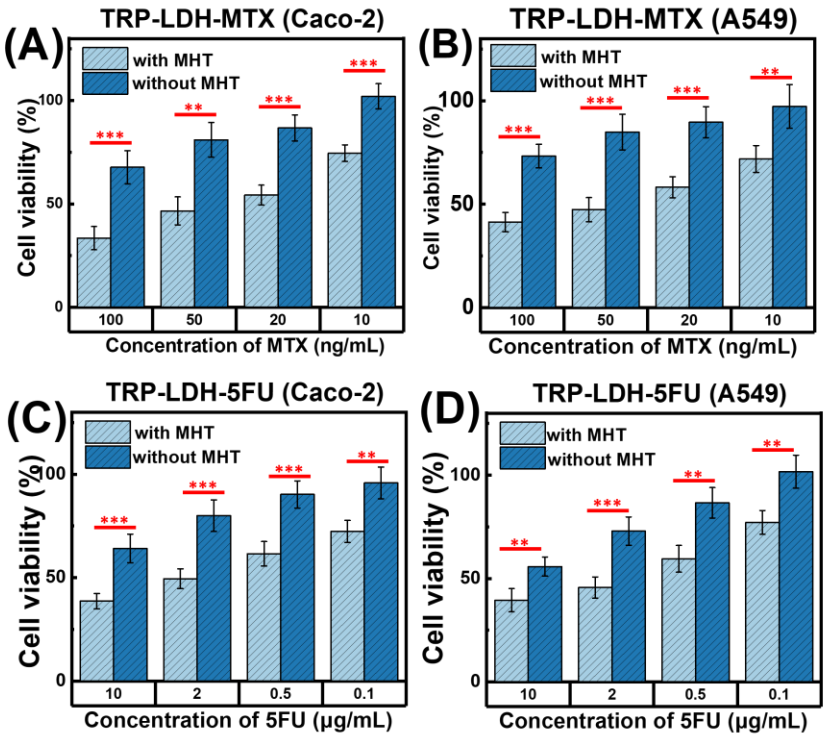

Fig. 6. *In vitro* cytotoxicity data: (A) Caco-2 and (B) A549 cells treated with TRP-LDH-MTX; (C) Caco-2 and (D) A549 cells treated with TRP-LDH-5FU. All cells were incubated with microparticles for 24 h, 37 °C with or without MHT (43°C, 60 min). Data given from four independent experiments as mean ± S.D. An untreated cells control is used as a baseline with a viability of 100%. **p<0.01, ***p<0.001. Cell viability data were compared by Student's t tests.

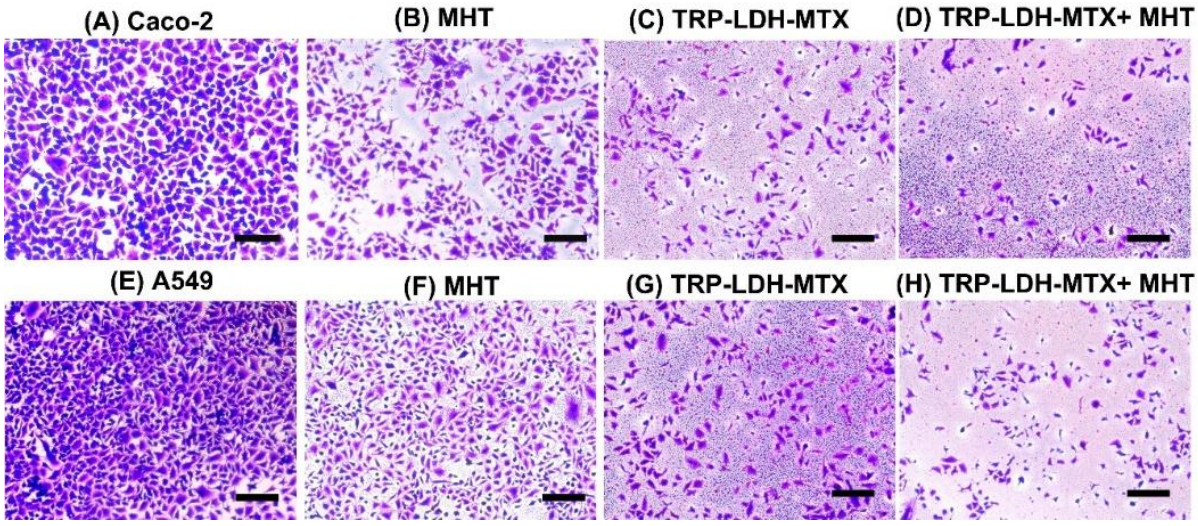

Fig. 7. Morphological changes reflecting visualized under a regular light microscope for: (A) Caco-2 cells and Caco-2 cells, and Caco-2 cells and Caco-2 cells treated with (B) MHT, (C) TRP-LDH-MTX and (D) MHT+TRP-LDH-MTX; (E) A549 cells, and A549 cells treated with (F) MHT, (G) TRP-LDH-MTX and (H) MHT+TRP-LDH-MTX (Scale bar: 100 μm). All cells were incubated for 24 h, 37 °C with or without MHT (43°C, 60 min).

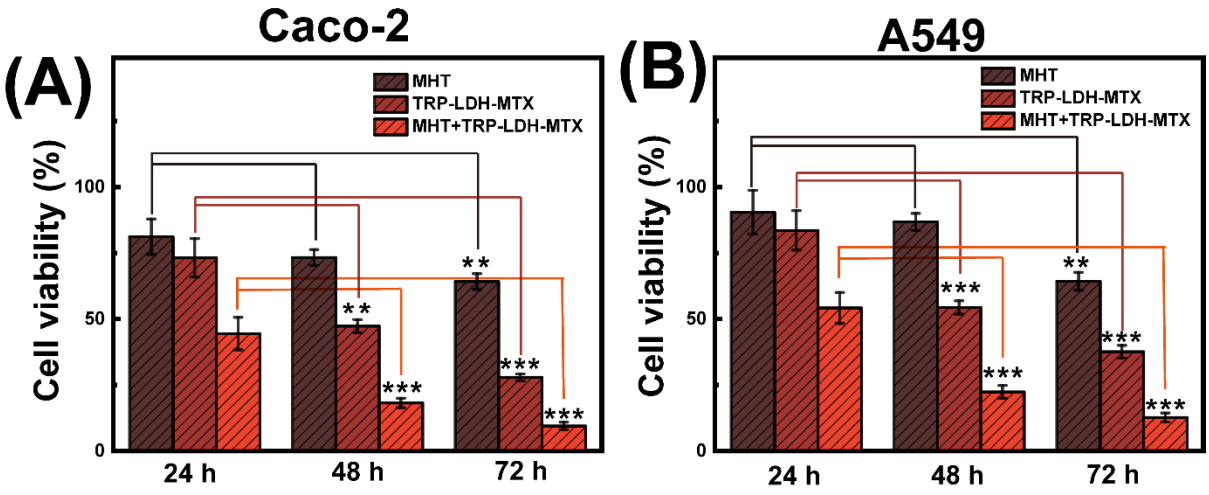

Fig. 8. *In vitro* cytotoxicity data for (A) Caco-2 and (B) A549 cells treated with TRP-LDH-MTX and multiple MHT (24, 48 and 72h, 37 °C; 1, 2, and 3 times, 43°C, 60 min, respectively). Data given from four independent experiments as mean ± S.D. An untreated cells control is used as a baseline with a viability of 100%. **p<0.01, ***p<0.001. Cell viability data were compared by Student's t tests.

Further studies exploiting a multiple MHT strategy were carried out to maximize the synergistic effects of our formulations with MHT. Hyperthermal treatment was induced every 24 h by elevating the temperature of an incubator to 43 °C. After 60 min of exposure, cells were immediately moved back to an incubator with temperature set at 37 °C. TRP-LDH-MTX was selected for these studies since it displayed the best anti-proliferation effects with MHT. Caco-2 and A549 cell lines were treated with TRP-LDH-MTX and exposed to high temperature (43 °C, 60 min) every 24 hours for three days. The results are given in Fig. 8. Clearly, when the MTH treatment was repeated, the cytotoxic effects of TRP-LDH-MTX are markedly enhanced, with a cell death rate greater than 80% after three MHT treatments. This presumably arises from an increased amount of MTX being freed from the microparticles with time, leading to enhanced chemotherapy aided by hyperthermia stress.

Previous studies have shown that a combination of hyperthermia and cytotoxic agents can synergistically inhibit the proliferation of Caco-2 and A549 cell lines [64-66]. In our study, we found that this synergy can be further amplified with the aid of our thermo-responsive TRP-LDH-drug formulations. The enhancement in synergistic effects can be explained by the following reasons. First, an increased amount of the chemotherapeutic was released from the TRP-LDH-drug systems at higher temperatures. Hyperthermia also promoted cell perfusion, facilitating the diffusion of 5FU or MTX into the cell membrane [67]. Finally, moderate heat treatment affects DNA repair mechanisms by inducing protein unfolding and exposing hydrophobic groups, resulting in aggregation and therefore promoting cell apoptosis after

chemotherapy [68, 69]. In a study with prostate cancer cells, a synergistic anti-proliferative effect was observed when 5FU was combined with moderate hyperthermia (43°C for 1 h), believed to result from inducible heat shock protein accumulation [70]. Similarly, higher cytotoxicity was obtained after exposing a tumor cell line to combined treatment with MTX and mild hyperthermia [71]. Such complementary hyperthermia can enhance the efficacy of DNA-damage-based chemotherapy by interfering with DNA repair response cascades and apoptosis induction [72].

4. Conclusions

In this work, we have successfully developed thermo-responsive theranostics for simultaneous MRI and controlled delivery of chemotherapeutic agents. These were generated by first incorporating drugs (5-fluorouracil and methotrexate, 5FU and MTX) into layered double hydroxide (LDH) nanoparticles, and then incorporating these with superparamagnetic iron oxide nanoparticles (SPIONs, MRI contrast agents) into in poly(acrylamide-co-acrylonitrile) microparticles. This polymer is thermoresponsive, and undergoes a globule-to-chain transition at around the physiological temperature. Microparticles with a concave shape were generated by spray drying, with elemental mapping indicating the SPIONs and LDH particles were homogenously distributed inside the formulations. The resultant nano-in-micro formulations displayed pH and thermosensitive *in vitro* drug release and relaxivity properties. Mathematical relationships could be elucidated to link drug release, temperature and the r_2 properties. *In vitro* cell culture models indicated that the microparticles can be used as thermo-responsive materials for hyperthermia-enhanced chemotherapy, with increased cell death noted when a short treatment at moderately elevated temperatures is paired with a chemotherapeutic. Hence, the formulations developed here could potentially be applied as theranostic platforms to improve therapeutic outcomes of hyperthermia and chemotherapy.

Acknowledgements

The authors gratefully thank Dr Andrew Weston and Dr Tom Gregory for assistance with electron microscopy and energy dispersive X-ray spectroscopy experiments. MMIR thanks the Missions sector in the Egyptian Ministry of Higher Education and the British Council Egypt for funding as a part of the Newton-Mosharafa scheme, as well as the Department of Chemistry at UCL for financial support. FLZ was supported by NIHR UCLH Biomedical Research Centre (BRC) grant, and UK-MRC ImagingBioPro grant (MR/R025673/1), and UCL Department of Medical Physics and Biomedical Engineering and EPSRC (EP/M020533/1; CMIC Pump-Priming Award).

References

[1]. S.K. Turan, H. Yildizhan, N.P. Barkan, F.D.Ö. Demiralp, B. Uslu, S.A. Ozkan
Novel diagnostic techniques: Genomic, proteomic and systems biology approaches. ***In Design of Nanostructures for Theranostics Applications***
William Andrew Publishing, (2018), pp. 1-40.

[2]. V.V. Mody, R. Siwale, A. Singh, H.R. Mody
Introduction to metallic nanoparticles
J. Pharm. Bioallied. Sci., 2 (2010), pp. 282.

[3]. S.S. Kelkar, T.M. Reineke
Theranostics: combining imaging and therapy
Bioconjug. Chem., 22 (2011), pp. 1879-1903.

[4]. E.K. Lim, T. Kim, S. Paik, S. Haam, Y.M. Huh, K. Lee
Nanomaterials for theranostics: recent advances and future challenges
Chem. Rev., 115 (2015), pp. 327-394.

[5]. X. Li, J. Kim, J. Yoon, X. Chen
Cancer-associated, stimuli-driven, turn on theranostics for multimodality imaging and therapy
Adv. Mater., 29 (2017), pp. 1606857.

[6]. H. Cai, Y. Xiang, Y. Zeng, Z. Li, X. Zheng, Q. Luo, Z. Gu, Y. Liu, H. Zhang, K. Luo
Cathepsin B-responsive and gadolinium-labeled branched glycopolymer-PTX conjugate-derived nanotheranostics for cancer treatment
Acta Pharm. Sin. B, 11 (2021), pp.544-559.

[7]. H. Cai, X. Dai, X. Wang, P. Tan, L. Gu, Q. Luo, X. Zheng, Z. Li, H. Zhu, H. Zhang, Z. Gu, Q. Gong, K. Luo
A nanostrategy for efficient imaging-guided antitumor therapy through a stimuli-responsive branched polymeric prodrug
Adv. Sci., 7 (2020), pp. 1903243.

[8]. P. Mi
Stimuli-responsive nanocarriers for drug delivery, tumor imaging, therapy and theranostics
Theranostics, 10 (2020), pp. 4557.

[9]. R. Zhu, W. Jiang, Y. Pu, K. Luo, Y. Wu, B. He, Z. Gu
Functionalization of magnetic nanoparticles with peptide dendrimers
J. Mater. Chem., 21 (2011), pp. 5464-5474.

[10]. Z. Zhang, C.J. Wells, A.M. King, J.C. Bear, G.L. Davies, G.R. Williams
pH-Responsive nanocomposite fibres allowing MRI monitoring of drug release.
J. Mater. Chem. B, 8 (2020), pp. 7264-7274.

[11]. D. Schmaljohann
Thermo-and pH-responsive polymers in drug delivery
Adv. Drug Deliv. Rev., 58 (2006), pp. 1655-1670.

[12]. M. Sethi, S. Chakarvarti
Hyperthermia techniques for cancer treatment: A review
Int. J. PharmTech. Res., 8 (2015), pp. 292-299.

[13]. M.M. Paulides, P.R. Stauffer, E. Neufeld, P.F. Maccarini, A. Kyriakou, R.A.M. Canters, C.J. Diederich, J.F. Bakker, G.C.V. Rhoon
Simulation techniques in hyperthermia treatment planning
Int. J. Hyperthermia, 29 (2013), pp. 346-357.

[14]. Y.Z. You, K.K. Kalebaila, S.L. Brock, D. Oupicky
Temperature-controlled uptake and release in PNIPAM-modified porous silica nanoparticles
Chem. Mater., 20 (2008), pp. 3354-3359.

[15]. T. Kawano, Y. Niidome, T. Mori, Y. Katayama, T. Niidome
PNIPAM gel-coated gold nanorods for targeted delivery responding to a near-infrared laser
Bioconjug. Chem., 20 (2009), pp. 209-212.

[16]. J. Lee, C.W. Macosko, D.W. Urry
Swelling behavior of γ-irradiation cross-linked elastomeric polypentapeptide-based hydrogels
Macromolecules, 34 (2001), pp. 4114-4123.

[17]. H.P. James, R. John, R., A. Alex, K. Anoop
Smart polymers for the controlled delivery of drugs–a concise overview
Acta Pharmacol. Sin. B, 4 (2014), pp. 120-127.

[18]. C.A. Quinto, P. Mohindra, S. Tong, G. Bao
Multifunctional superparamagnetic iron oxide nanoparticles for combined chemotherapy and hyperthermia cancer treatment
Nanoscale, 7 (2015), pp. 12728-12736.

[19]. H. Wang, P. Agarwal, Y. Xiao, H. Peng, S. Zhao, X. Liu, S. Zhou, J. Li, J. Liu, X. He
A nano-in-micro system for enhanced stem cell therapy of ischemic diseases
ACS Cent. Sci., 3 (2017), pp. 875-885.

[20]. P. Nalawade, B. Aware, V.J. Kadam, R.S. Hirlekar,
Layered double hydroxides: A review.
CSIR, 2009

[21]. G. Choi, S. Eom, A. Vinu, A., J.H. Choy
2D nanostructured metal hydroxides with gene delivery and theranostic functions; a comprehensive review
Chem. Rec., 18 (2018), pp. 1033-1053.

[22]. Z. Cao, B. Li, L. Sun, L. Li, Z.P. Xu, Z. Gu
2D layered double hydroxide nanoparticles: recent progress toward preclinical/clinical nanomedicine
Small Methods, 4 (2020), pp. 1900343.

[23]. L. Yan, S. Gonca, G. Zhu, W. Zhang, X. Chen
Layered double hydroxide nanostructures and nanocomposites for biomedical applications
J. Mater. Chem. B, 7 (2019), pp. 5583-5601.

[24]. S. Niu, G.R. Williams, J. Wu, X. Zhang, H. Zheng, S. Li, L.M. Zhu
A novel chitosan-based nanomedicine for multi-drug resistant breast cancer therapy
Chem. Eng. J., 369 (2019), pp. 134-149.

[25]. M. Hoekstra, C. Haagsma, C. Neef, J. Proost, A. Knuif, M. van de Laar
Bioavailability of higher dose methotrexate comparing oral and subcutaneous administration in patients with rheumatoid arthritis
J. Rheumatol., 31 (2004), pp. 645-648.

[26]. E.N. Van Roon, M. Van de Laar
Methotrexate bioavailability
Clin. Exp. Rheumatol. - Incl Supplements, 28 (2010), pp. S27.

[27]. M. Gusella, A. Frigo, C. Bolzonella, R. Marinelli, C. Barile, A. Bononi, G. Crepaldi, D. Menon, L. Stievano, S. Toso, F. Pasini, E. Ferrazzi, R. Padrini
Predictors of survival and toxicity in patients on adjuvant therapy with 5-fluorouracil for colorectal cancer
Br. J. Cancer, 100 (2009), pp. 1549-1557.

[28]. R. Han, Y.M. Yang, J., Dietrich, A. Luebke, M. Mayer-Pröschel, M. Noble
Systemic 5-fluorouracil treatment causes a syndrome of delayed myelin destruction in the central nervous system
J. Biol. 7 (2008), pp. 1-22.

[29]. X. Sun, C. Liu, A.M. Omer, W. Lu, S. Zhang, X. Jiang, H. Wu, D. Yu, X.K. Ouyang, X. K.
pH-sensitive ZnO/carboxymethyl cellulose/chitosan bio-nanocomposite beads for colon-specific release of 5-fluorouracil
Int. J. Biol. Macromol., 128 (2019), pp. 468-479.

[30]. Z. Liu, S. Rimmer
Synthesis and release of 5-fluorouracil from poly (N-vinylpyrrolidinone) bearing 5-fluorouracil derivatives
J. Controlled Release, 81 (2002), pp. 91-99.

[31]. B. Li, Z. Gu, N. Kurniawan, W. Chen, Z.P. Xu
Manganese-based layered double hydroxide nanoparticles as a T_1-MRI contrast agent with ultrasensitive pH response and high relaxivity
Adv. Mater., 29 (2017), pp. 1700373.

[32]. M. Hei, J. Wang, K. Wang, W. Zhu, P.X. Ma
Dually responsive mesoporous silica nanoparticles regulated by upper critical solution temperature polymers for intracellular drug delivery
J. Mater. Chem. B, 5 (2017), pp. 9497-9501.

[33]. Y. Wang, Z. Zhang, Y. Abo-zeid, J.C. Bear, G.L. Davies, X. Lei, G.R. Williams
SiO2-coated layered gadolinium hydroxides for simultaneous drug delivery and magnetic resonance imaging
J. Solid State Chem., 286 (2020), pp. 121291.

[34]. L. Li, Z. Gu, W. Gu, J. Liu, Z.P. Xu
Efficient drug delivery using SiO2-layered double hydroxide nanocomposites
J. Colloid Interface Sci., 470 (2016), pp. 47-55.

[35]. J. Chakraborty, S. Roychowdhury, S. Sengupta, S. Ghosh
Mg–Al layered double hydroxide–methotrexate nanohybrid drug delivery system: evaluation of efficacy
Mater. Sci. Eng. C, 33 (2013), pp. 2168-2174.

[36]. Z. Wang, E. Wang, L. Gao, L. Xu
Synthesis and properties of Mg2Al layered double hydroxides containing 5-fluorouracil
J. Solid State Chem., 178 (2005), pp. 736-741.

[37]. G. Tuncelli, G., Ay, A.N. Ay, B. Zümreoglu-Karan
5-Fluorouracil intercalated iron oxide@ layered double hydroxide core-shell nano-composites with isotropic and anisotropic architectures for shape-selective drug delivery applications
Mater. Sci. Eng. C, 55 (2015), pp. 562-568.

[38]. A.R. de Oliveira, E.F. Molina, P. de C. Mesquita, J.L.C. Fonseca, G. Rossanezi, M. de F. Fernandes-Pedrosa, A.G. de Oliveira, A.A. da Silva-Júnior
Structural and thermal properties of spray-dried methotrexate-loaded biodegradable microparticles
J. Therm. Anal. Calorim., 112 (2012), pp. 555-565.

[39]. Singh, G. Van den Mooter
Spray drying formulation of amorphous solid dispersions
Adv. Drug Deliv. Rev., 100 (2016), pp. 27-50.

[40]. V. Avasatthi, H. Pawar, C.P. Dora, P. Bansod, M.S. Gill, S. Suresh
A novel nanogel formulation of methotrexate for topical treatment of psoriasis: optimization, in vitro and in vivo evaluation
Pharm. Dev. Technol., 21(2016), pp. 554-562.

[41]. M. Chakraborty, S. Dasgupta, S. Sengupta, J. Chakraborty, S. Ghosh, J. Ghosh, M. K. Mitra A. Mishra, T.K. Mandal, D. Basu
A facile synthetic strategy for Mg–Al layered double hydroxide material as nanocarrier for methotrexate
Ceram. Int., 38 (2012), pp. 941-949.

[42]. Q.J. Huang, H.Y. Zeng, W. Zhang, B. Feng, X.J. Liu, H.Z. Duan, P.X. Ding
Loading kinetics of 5-fluorouracil onto hydrotalcite and in vitro drug delivery
J. Taiwan Inst. Chem. Eng., 60 (2016), pp. 525-531.

[43]. Y. Cheng, S. Weng, L. Yu, N. Zhu, M. Yang, Y. Yuan, Y
The role of hyperthermia in the multidisciplinary treatment of malignant tumors
Integr. Cancer Ther., 18 (2019).

[44]. B.V. Harmon, Y.S. Takano, C.M. Winterford, G.C. Gobe
The role of apoptosis in the response of cells and tumours to mild hyperthermia
Int. J. Radiat. Oncol. Biol. Phys., 59 (1991), pp. 489-501.

[45]. V. Saxena
Temperature distribution in human skin and subdermal tissue
J. Theor. Biol., 102 (1983), pp. 277-286.

[46]. C.P. Chen, R.L. Hwang, S.Y. Chang, Y.T. Lu
Effects of temperature steps on human skin physiology and thermal sensation response
Build. Environ., 46 (2011), 2387-2397.

[47]. M. Rabinovitch
Professional and non-professional phagocytes: an introduction
Trends Cell Biol., 5(1995), pp. 85-7.

[48]. J.L. Vivero‐Escoto, I.I. Slowing, B.G. Trewyn, VSY. Lin,
Mesoporous silica nanoparticles for intracellular controlled drug delivery
Small, 6 (2010), pp. 1952-1967.

[49]. A. Prokop, J.M. Davidson
Nanovehicular intracellular delivery systems
J. Pharm. Sci., 97 (2008), pp. 3518-90.

[50]. Y. Gao, T.W. Teoh, Q. Wang, G.R. Williams
Electrospun organic-inorganic nanohybrids as sustained release drug delivery systems
J. Mater. Chem. B, 2017. 5 (2017), pp. 9165-9174.

[51]. V. Rives, M. Del Arco, C. Martín
Layered double hydroxides as drug carriers and for controlled release of non-steroidal antiinflammatory drugs (NSAIDs): a review
J. Controlled Release, 169 (2013), pp. 28-39.

[52]. V. Rives, M. Del Arco, C. Martín
Intercalation of drugs in layered double hydroxides and their controlled release: A review
Appl. Clay Sci., 88 (2014), pp. 239-269.
[53]. P.L. Ritger, N.A. Peppas
A simple equation for description of solute release II. Fickian and anomalous release from swellable devices
J. Control Release, 5 (1987), pp. 37-42.

[54]. D.S. Simmons, I.C. Sanchez
Scaled particle theory for the coil–globule transition of an isolated polymer chain
Macromolecules, 46(2013), pp. 4691-4697.

[55]. J. Moore, H.H. Flanner
Mathematical comparison of dissolution profiles
Pharm. Technol., 20 (1996), pp. 64-74.

[56]. G. Freitag
Guidelines on dissolution profile comparison
Drug Information J., 35(2001), pp. 865-874.

[57]. J. van der Zee, D. González, G.C. van Rhoon, J.D. van Dijk, W.L. van Putten, A.A. Hart
Comparison of radiotherapy alone with radiotherapy plus hyperthermia in locally advanced pelvic tumours: a prospective, randomised, multicentre trial
Lancet, 355 (2020), pp. 1119-1125.

[58]. R.D. Issels, et. al

Neo-adjuvant chemotherapy alone or with regional hyperthermia for localised high-risk soft-tissue sarcoma: a randomised phase 3 multicentre study
Lancet Oncol., 11 (2010), pp. 561-570.

[59]. C.W. Song
Effect of local hyperthermia on blood flow and microenvironment: a review
Cancer Res., 44(1984), pp. 4721s-4730s.

[60]. P. M. Krawczyk, et. al
Mild hyperthermia inhibits homologous recombination, induces BRCA2 degradation, and sensitizes cancer cells to poly (ADP-ribose) polymerase-1 inhibition
PNAS, *108*(2011), pp. 9851-9856.

[61]. Z. Zoul, S. Filip, B. Melichar, J. Dvořák, K. Odrážka, J. Petera
Weekly paclitaxel combined with local hyperthermia in the therapy of breast cancer locally recurrent after mastectomy–a pilot experience
Oncol. Res. Treat., 27(2004), pp. 385-388.

[62]. R.J. Griffin, R.P. Dings, A. Jamshidi-Parsian, C.W. Song
Mild temperature hyperthermia and radiation therapy: role of tumour vascular thermotolerance and relevant physiological factors
Int. J. Hyperthermia, 26 (2010), pp. 256-263.

[63]. M.G. Santoro
Heat shock proteins and virus replication: hsp70s as mediators of the antiviral effects of prostaglandins
Experientia, 50(1994), pp. 1039-1047.

[64]. H.L. Rodríguez-Luccioni, M. Latorre-Esteves, J. Méndez-Vega, O. Soto, A.R. Rodríguez, C. Rinaldi, M. Torres-Lugo
Enhanced reduction in cell viability by hyperthermia induced by magnetic nanoparticles
Int. J. Nanomed., 6 (2011), pp. 373.

[65]. M.P. Alvarez-Berríos, A. Castillo, C. Rinaldi, M. Torres-Lugo
Magnetic fluid hyperthermia enhances cytotoxicity of bortezomib in sensitive and resistant cancer cell lines
Int. J. Nanomed., 9 (2014), pp. 145.

[66]. J. Park, S.H. Baek
Combination therapy with cinnamaldehyde and hyperthermia induces apoptosis of a549 non-small cell lung carcinoma cells via regulation of reactive oxygen species and mitogen-activated protein kinase family
Int. J. Mol. Sci., 21 (2020), pp. 6229.

[67]. S. Jha, P.K. Sharma, R. Malviya
Hyperthermia: role and risk factor for cancer treatment
Achiev. Life Sci., 10 (2016), pp. 161-167.

[68]. G.G. Jonsson, G. Eriksson, R.W. Pero
Effects of γ radiation and hyperthermia on DNA repair synthesis and the level of NAD+ in cultured human mononuclear leukocytes
Radiat. Res., 97 (1984), pp. 97-107.

[69]. B. Eppink, P.M. Krawczyk, J. Stap, R. Kanaar
Hyperthermia-induced DNA repair deficiency suggests novel therapeutic anti-cancer strategies
Int. J. Hyperthermia, 28 (2012), pp. 509-517.

[70]. J. Roigas, E.S. Wallen, S.A. Loening, P.L. Moseley
Effects of combined treatment of chemotherapeutics and hyperthermia on survival and the regulation of heat shock proteins in Dunning R3327 prostate carcinoma cells
The Prostate, 34 (1988), pp. 195-202.

[71]. M. Stapf, N. Pömpner, U. Teichgräber, I. Hilger
Heterogeneous response of different tumor cell lines to methotrexate-coupled nanoparticles in presence of hyperthermia
Int. J. Nanomedicine, 11 (2016), pp. 485.

[72]. T. Mantso, G. Goussetis, R. Franco, S. Botaitis, A. Pappa, M. Panayiotidis
Effects of hyperthermia as a mitigation strategy in DNA damage-based cancer therapies
Semin. Cancer Biol., 37 (2016), pp. 96-105